Organic semiconducting polymer nanoparticles for photoacoustic labeling and tracking of stem cells in the second near-infrared window

Yin, Chao; Wen, Guohua; Liu, Chao; Yang, Boguang; Lin, Sien; Huang, Jiawei; Zhao, Pengchao; Wong, Dexter Siu Hong; Zhang, Kunyu; Chen, Xiaoyu; Li, Gang; Jiang, Xiaohua; Huang, Jianping; Pu, Kanyi; Wang, Lidai; Bian, Liming

2018

Yin, C., Wen, G., Liu, C., Yang, B., Lin, S., Huang, J., . . . Bian, L. (2018). Organic semiconducting polymer nanoparticles for photoacoustic labeling and tracking of stem cells in the second near-infrared window. ACS Nano, 12(12), 12201-12211. doi:10.1021/acsnano.8b05906

https://hdl.handle.net/10356/137150

https://doi.org/10.1021/acsnano.8b05906

Organic Semiconducting Polymer Nanoparticles for Photoacoustic Labelling and Tracking of Stem Cells in the Second Near-Infrared Window

Chao Yin,[†,||] *Guohua Wen,*[‡,||] *Chao Liu,*[‡,||] *Boguang Yang,*[†] *Sien Lin,*[¶,§,¤] *Jiawei Huang,*[&] *Pengchao Zhao,*[†] *Siu Hong Dexter Wong,*[†] *Kunyu Zhang,*[†] *Xiaoyu Chen,*[†] *Gang Li,*[¶, §,^] *Xiaohua Jiang,*[&] *Jianping Huang,*[¶] *Kanyi Pu,*[*,#] *Lidai Wang,*[*,‡,°] *and Liming Bian*[*,†,¤,+,•]

[†]Department of Biomedical Engineering, The Chinese University of Hong Kong, Shatin, New Territories, Hong Kong, China

[‡]Department of Biomedical Engineering, City University of Hong Kong, 83 Tat Chee Ave, Kowloon, Hong Kong, China

[¶]Department of Orthopaedics & Traumatology, Faculty of Medicine, The Chinese University of Hong Kong, Prince of Wales Hospital, Shatin, Hong Kong, China

[§]Stem Cells and Regenerative Medicine Laboratory, Lui Che Woo Institute of Innovative Medicine, Li Ka Shing Institute of Health Sciences, The Chinese University of Hong Kong, Prince of Wales Hospital, Shatin, Hong Kong, China

[¤]Department of Pharmacology, Guangdong Key Laboratory for Research and Development of Natural Drugs, Guangdong Medical University, Zhanjiang, Guangdong 510000, China

[&]School of Biomedical Sciences, Faculty of Medicine, The Chinese University of Hong Kong, Hong Kong, China

[^]The CUHK-ACC Space Medicine Centre on Health Maintenance of Musculoskeletal System, The Chinese University of Hong Kong Shenzhen Research Institute, Shenzhen 518172, China

[#]School of Chemical and Biomedical Engineering, Nanyang Technological University, 70 Nanyang Drive, 637457 Singapore

[°]City University of Hong Kong Shenzhen Research Institute, Yuexing Yi Dao, Nanshan District, Shenzhen, Guang Dong, 518057, China

[+]Shenzhen Research Institute, The Chinese University of Hong Kong, Shenzhen 518172, China

[•]China Orthopedic Regenerative Medicine Group (CORMed), Hangzhou, Zhejiang 310058, China

[*]Address correspondence to:

kypu@ntu.edu.sg

lidawang@cityu.edu.hk

lbian@cuhk.edu.hk

ABSTRACT: Photoacoustic (PA) imaging and tracking of stem cells plays an important role in the real-time assessment of cell-based therapies. Nevertheless, the limitations of conventional inorganic PA contrast agents and the narrow range of the excitation wavelength in the first near-infrared (NIR-I) window hamper the applications of PA imaging in living subjects. Herein we report the design and synthesis of a second near-infrared (NIR-II) absorptive organic semiconducting polymer (OSP)-based nanoprobe ($OSPN^+$) for PA imaging and tracking of stem cells. Comparison studies in biological tissue showed that NIR-II light excited PA imaging of the $OSPN^+$ had significantly higher signal-to-noise ratio (SNR) than NIR-I light excited PA imaging, thereby demonstrating the superiority of the $OSPN^+$ for deep tissue imaging. With good biocompatibility, appropriate size, and optimized surface property, the $OSPN^+$ showed enhanced cellular uptake for highly efficient PA labelling of stem cells. *In vivo* investigations revealed significant NIR-II PA contrast enhancement of the transplanted $OSPN^+$-labelled human mesenchymal stem cells (hMSCs) by 40.6- and 21.7-fold in subcutaneous and brain imaging, respectively, compared with unlabelled cases. Our work demonstrates a class of OSP-based nanomaterials for NIR-II PA stem cell imaging to facilitate a better understanding and evaluation of stem cell-based therapies.

KEYWORDS: organic semiconducting polymer, nanoparticle, stem cell, second near-infrared absorption, photoacoustic imaging.

Human mesenchymal stem cells (hMSCs) have attracted tremendous attention in the clinical medicine field due to their multipotency to differentiate into diversified mesenchymal lineages, such as osteoblasts, chondrocytes, and adipocytes.[1] This multipotency of hMSCs offers promising potential in regenerative medicine, which focuses on the repair and regeneration of injured and damaged tissues.[2,3] Diverse imaging techniques, including fluorescence imaging (FI),[4-6] magnetic resonance imaging (MRI),[7-9] and positron emission tomography (PET),[10,11] have been utilized for stem cell imaging and tracking. However, each of these imaging modalities has its own pros and cons. For instance, although FI can reveal biological information with high sensitivity, it has limited tissue penetration depth and strong photon scattering in living subjects. MRI has high spatial resolution and imaging contrast, but its temporal resolution is relatively poor,[12-14] which limits the application for monitoring transplanted cells. Therefore, developing complementary techniques for labelling and tracking of stem cells is of great significance and in high demand.

Photoacoustic (PA) imaging is a nonionizing and non-invasive imaging technique that takes advantage of both light excitation and acoustic detection in a single imaging modality.[15-21] Compared with traditional optical imaging, PA imaging can provide a much greater imaging depth [15,22] as well as superior temporal resolution (100 ms),[14] and these advantages make PA imaging an ideal modality for *in vivo* applications. Other investigations have reported PA imaging-guided stem cell transplantation in living animals, demonstrating it as a promising direction. Nevertheless, two significant problems remain unaddressed. First, the PA contrast agents used in almost all the prior studies are inorganic nanoprobes such as Prussian Blue[14] and gold nanoparticles,[23-25] which need further evaluation on biodegradation and long-term toxicity. Second, the currently used PA imaging technology primarily employed a short near-infrared (NIR) light (NIR-I, 650-950 nm) to generate PA signals. However, PA imaging conducted in the second NIR window (NIR-II, 1000-1700 nm) has distinct superiorities including deeper tissue penetration and higher maximum permissible exposure (MPE) to laser compared with NIR-I imaging.[18] Besides, 1064 nm laser excited NIR-II PA imaging shows much higher signal-to-noise ratio (SNR) relative to NIR-I PA imaging at 800 or 900 nm.[26] Unfortunately, NIR-II PA imaging has rarely been reported, not to mention its application in stem cell studies.

Organic semiconducting polymer nanoparticles (OSPNs) prepared from semiconducting polymers (SPs) are promising nanoagents with excellent optical properties for imaging and therapy.[27-31] Regarding to their various superiorities, such as excellent optical properties, good biocompatibility, and higher photothermal conversion efficiency compared with some inorganic nanomaterials, OSPNs have been widely utilized for fluorescence,[32-35] chemiluminescence,[36,37] afterglow[38,39] and photoacoustic imaging,[40-44] as well as photothermal[45,46] and photodynamic therapies.[47] Furthermore, the structural versatility of SPs allows the preparation of OSPNs with different absorption bands ranging from the ultraviolet to NIR region, even extending to the NIR-II window. Although one study has reported the PA imaging of embryonic stem cell-derived cardiomyocytes using OSPNs, the excitation wavelength was still restricted to the NIR-I region, thereby limiting the imaging depth.[48] Pu’s group first reported the utilization of OSPNs for rat brain PA imaging in both NIR-I and NIR-II window and demonstrated the superiority of NIR-II over NIR-I PA imaging with a higher SNR.[18] Therefore, development of NIR-II absorptive OSPNs as PA contrast agents is of great importance for PA imaging and tracking of stem cells in deep biological tissue.

In this work, we report the design and preparation of positively charged OSPNs (OSPNs$^+$) for stem cell PA imaging and tracking in the NIR-II window (Figure 1a). The architecture of the OSPNs$^+$ comprises three components: a hydrophobic semiconducting polymer (SP) core, an anionic interlayer, and a cationic shell. The SP core acts as the PA signal producer under NIR-I or NIR-II laser excitation, which was encapsulated by amphiphilic poly (styrene maleic anhydride) (PSMA) to obtain the water-dispersed nanoparticles (OSPNs$^-$) with an anionic surface for further modification. Poly(L-lysine) (PLL) was subsequently adsorbed onto the OSPNs$^-$ surface *via* electrostatic interactions to enhance the cellular uptake of the obtained cationic nanoparticles (OSPNs$^+$). We first described the synthesis and characterizations of the SP and OSPNs$^+$, then investigated the optical and PA properties of OSPNs$^+$ in solution. Then, PA imaging of stem cells by using the OSPNs$^+$ was proved effective *in vitro*. Based on the superior PA imaging effects excited by NIR-II light compared with the results obtained from NIR-I light excitation, we further demonstrated the PA labelling and tracking of hMSCs in living mice in the NIR-II region.

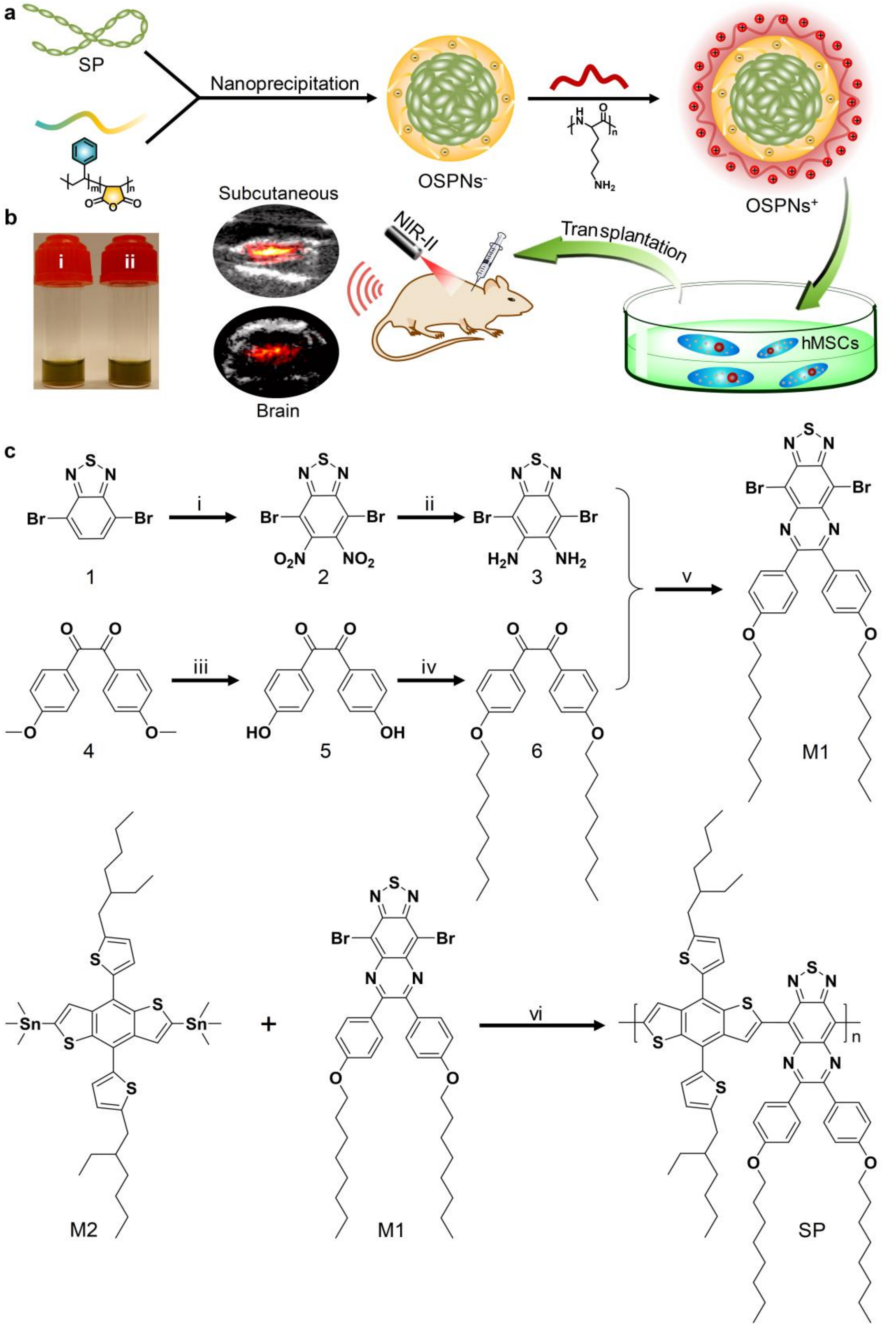

Figure 1. a) Illustration of the preparation procedure of OSPNs$^+$ and the photoacoustic labelling of hMSCs after transplantation. b) Photograph of the OSPNs$^-$ (i) and OSPNs$^+$ (ii) aqueous solutions. c) Illustration of the synthetic route of the semiconducting polymer (SP). Reaction conditions: (i) sulfuric acid, nitric acid,

100°C; (ii) iron powder, acetic acid, 80°C; (iii) pyridine hydrochloride, H_2O, 220 to 80°C; (iv) 1-bromooctane, potassium carbonate, acetone, reflux; (v) acetic acid, N_2, 135°C; (vi) tri(o-tolyl)phosphine, tris(dibenzylideneacetone)dipalladium(0), toluene, N_2, 100°C.

RESULTS AND DISCUSSION

The SP was synthesized *via* Pd-catalysed Stille coupling polymerization (Figure 1c). We chose this electron donor (D)-acceptor (A) pair to construct the conjugated backbone because thiadiazoloquinoxaline-based polymers generally possess a low band gap because of the strong electron-withdrawing capability of the thiadiazoloquinoxaline unit, thus resulting in the NIR-II absorption.[18] The monomer 1 (M1) was prepared *via* the modified route according to previous literatures.[49,50] In brief, 4,7-dibromo-2,1,3-benzothiodiazole (1) was first treated with sulfuric acid and nitric acid to yield compound 2. Then, iron powder was utilized to reduce the nitro of 2 in acetic acid media, affording compound 3. As a parallel route, compound 5 was first synthesized by heating the mixture of 1,2-bis(4-methoxyphenyl)ethane-1,2-dione (4) and pyridine hydrochloride at 220°C to convert the methoxy group ($-OCH_3$) to a hydroxyl (-OH) group. Then, compound 5 was alkylated with 1-bromooctane in the presence of potassium carbonate (K_2CO_3) to obtain compound 6. M1 was subsequently obtained *via* stirring the mixture of compound 3 and 6 in acetic acid solution at 135 °C under nitrogen protection for 24 h. At last, Pd-catalysed Stille coupling polymerization between M1 and M2 was performed to construct the conjugated backbone, yielding the product (SP). NMR and mass spectra were utilized to confirm the correct structures of all the intermediates and final product (Figures S1-S5 & Table S1, Supporting Information). For the SP, the resonance peak at 8.9

ppm is attributed to the hydrogen signal from the thiophene ring adjacent to thiadiazoloquinoxaline unit, and the resonance peak at 4.1 ppm is assigned to the methylene-H attached to the oxygen ($-O-CH_2$) of thiadiazoloquinoxaline segment (Figure S4, Supporting Information). This result indicated the successful linkage between M1 and M2, generating the expected product (SP). Furthermore, the resonance peaks assigned to the hydrogen signal of the aromatic ring (benzene ring and thiophene ring) and alkyl chains shifted noticeably to 6.5-8.0 ppm and 0.5-2.5 ppm, respectively (Figure S4, Supporting Information). Gel permeation chromatograph (GPC) results showed a high molecular weight (Mn = 39800 Da, Mw = 50100 Da) of SP with a relatively narrow polydispersity index (PDI) of 1.26 (Figure S5 & Table S1, Supporting Information). All these results clearly verified the successful synthesis of SP.

The $OSPNs^+$ were prepared *via* two steps (Figure 1a). The nanoprecipitation of SP and PSMA was first employed to produce carboxyl-decorated nanoparticles ($OSPNs^-$) with a large negative surface charge (zeta potential: -49.8 ± 4.0 mV, Figure 2c). For efficient cell internalization, poly(L-lysine) (PLL), a widely used cationic polymer for stem cell imaging,[14,51,52] was further employed to modify the $OSPNs^-$ surface to convert the nanoparticle surface to a positive charge ($OSPNs^+$) with a zeta potential of +42 ± 6.6 mV (Figure 2c). Both the $OSPNs^-$ and $OSPNs^+$ aqueous solutions exhibited the similar olive colour (Figure 1b). Transmission electron microscopy (TEM) revealed that the $OSPNs^+$ and the $OSPNs^-$ were spherical morphology (Figure 2a & Figure S6, Supporting Information). Dynamic light scattering (DLS) indicated the mean hydrodynamic diameter of the OSPNs$^+$ at 113.2 ± 4.8 nm, which is slightly larger than that of the OSPNs$^-$ (average diameter: 99.9 nm) (Figure 2b). The average size of the OSPNs$^+$ remained almost the same even after storage in aqueous media or 10% fetal bovine serum (FBS) solution for one month (Figures S7 & S8, Supporting Information), indicating the high colloidal stability of the nanoparticles. This is mainly due to the electrostatic repulsion among the nanoparticles provided by the positively charged PLL shell of the OSPNs$^+$ and the structural integrity provided by the strong hydrophobic interactions and π-π stacking between the SP and the hydrophobic segment of PSMA.

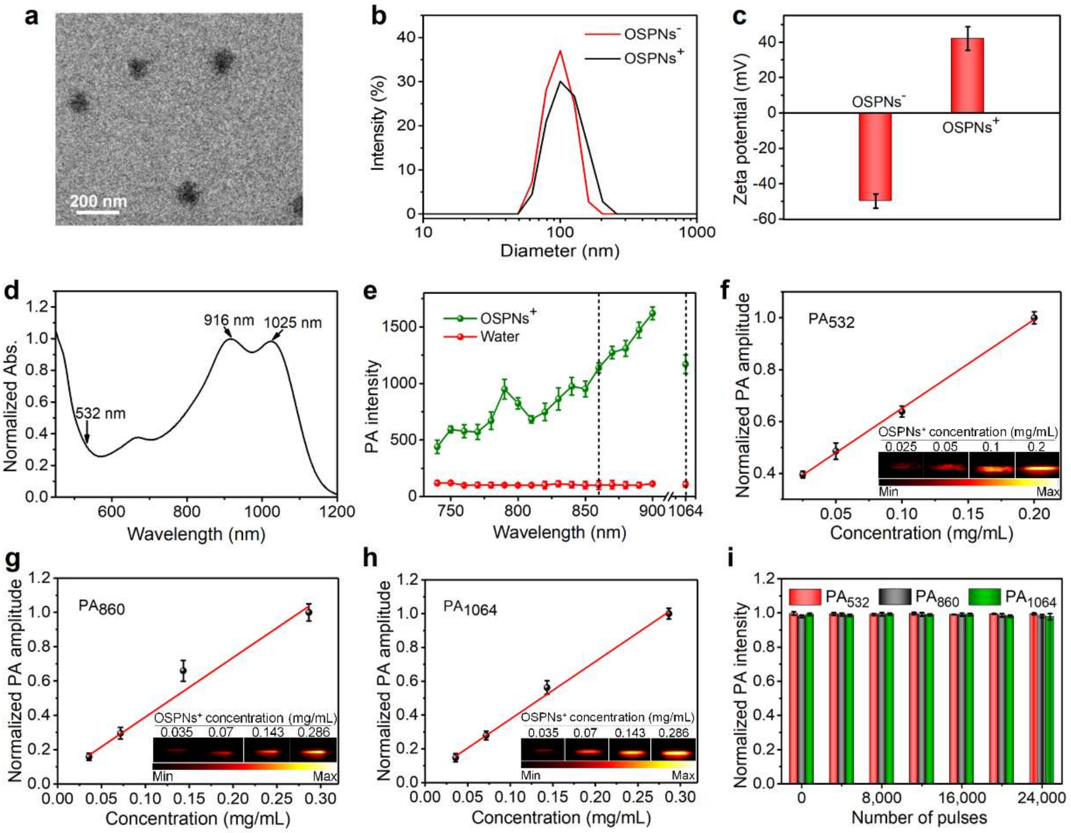

Figure 2. Characterizations of the OSPNs$^+$. a) Representative TEM image of the nanoparticles (OSPNs$^+$). b) DLS results of the OSPNs$^-$ and OSPNs$^+$. c) Zeta potential of the OSPNs$^-$ and OSPNs$^+$ in aqueous solution. d) Normalized absorption spectrum of the OSPNs$^+$ in aqueous media. e) PA spectra of the OSPNs$^+$ (0.573 mg/mL) and pure water. Normalized PA intensity of the OSPNs$^+$ at 532 nm (PA_{532}) (f), 860 nm

(PA_{860}) (g), and 1064 nm (PA_{1064}) (h) as a function of concentration. Inset: PA imaging of OSPNs$^+$ under different concentrations. i) Normalized PA intensity of the OSPNs$^+$ (0.1 mg/mL) at 532 nm, 860 nm, and 1064 nm under laser excitation at 532 nm, 860 nm, and 1064 nm, respectively, with varying laser pulses (5.0 mJ/cm^2).

The optical properties of the OSPNs$^+$ were investigated by measuring the absorption spectra in aqueous media. Compared with the absorption of SP in tetrahydrofuran which exhibited the highest absorption peak at 990 nm with a vibronic band shoulder at 892 nm (Figure S9, Supporting Information), the OSPNs$^+$ showed two absorption peaks, at 916 nm and 1025 nm in the NIR region, with almost identical absorption intensities (Figure 2d). In addition, a high molar absorption coefficient of 1.01×10^6 $M^{-1}cm^{-1}$ was calculated by correlating the absorption intensity at 1025 nm as a function of OSPNs$^+$ concentration in the aqueous media (Figure S10, Supporting Information), and this reflects the promising potential of OSPNs$^+$ for PA imaging in the NIR-II window. Furthermore, the OSPNs$^+$ exhibited excellent photostability as shown by the absorbance fluctuation test under NIR-II light (1064 nm) irradiation for 30 min (Figure S11, Supporting Information), indicating the feasibility of using OSPNs$^+$ for long-term imaging applications.

The photoacoustic properties of the OSPNs$^+$ were investigated in aqueous solution. Because OSPNs$^+$ have a broadband absorption profile covering both the NIR-I and NIR-II regions, they also exhibit strong NIR-I and NIR-II PA signals (Figure 2e). Pure water was used as the control and showed minimal PA signals (Figure 2e). It should be noted that the PA intensity of the OSPNs$^+$ at 860 nm is almost identical to that at 1064 nm, consistent with the absorption profile (Figure 2e *vs.* Figure 2d). The PA intensity of the OSPNs$^+$ collected at 532 nm, 860 nm, and 1064 nm increased linearly with increasing concentration (Figures 2f-2h), and this demonstrates the feasibility of signal quantification. In addition, the PA intensity of the $OSPNs^+$ remained almost unchanged even after exposure to 24000 laser pulses (Figure 2i), thereby showing the excellent stability and feasibility of long-term PA tracking both *in vitro* and *in vivo*.

We next evaluated the $OSPNs^+$ for PA labelling of stem cells. MTT assay showed that both the $OSPNs^+$ and $OSPNs^-$ had little effect on cellular metabolic activities at a relatively high concentration (50 μg/mL) (Figure 3a, Figure S12, Supporting Information). Optical-resolution photoacoustic microscopy (OR-PAM) revealed that the $OSPNs^+$ can be efficiently internalized into hMSCs to emit a strong PA signal in the cytoplasm while clearly showing the nuclei with a low signal (Figure 3b). In contrast, relatively weak PA signals were detected from hMSCs treated with the $OSPNs^-$ (Figure 3b). Quantification data reflected that the average number of internalized nanoparticles into one single cell was 127.5 pg/cell (25.5% of the added $OSPNs^+$) and 39.6 pg/cell (7.92% of the added $OSPNs^-$) for $OSPNs^+$ and $OSPNs^-$, respectively. Imaging quantification further indicated that the PA signal intensity of $OSPNs^+$-treated cells was ~3-fold higher than that of $OSPNs^-$-treated cells (Figure S13, Supporting Information). This can be explained from the positively charged surfaces of the $OSPNs^+$ that facilitated the interactions between the nanoparticles and the negatively charged cell membrane. To further evaluate the labelling efficacy, stem cells were treated with the $OSPNs^+$ and then collected to monitor their PA emissions (Figure 3c). After incubating for 12 h with the $OSPNs^+$, PA imaging of the cell pellets at both 860 and 1064 nm showed an obvious signal enhancement, which exhibited

~3-fold brighter relative to the OSPNs$^-$-labelled cell pellets (Figure 3d, Figure S14, Supporting Information), and this was consistent with the OR-PAM results. These data demonstrate the potential of the OSPNs$^+$ for stem cell imaging and tracking in living subjects.

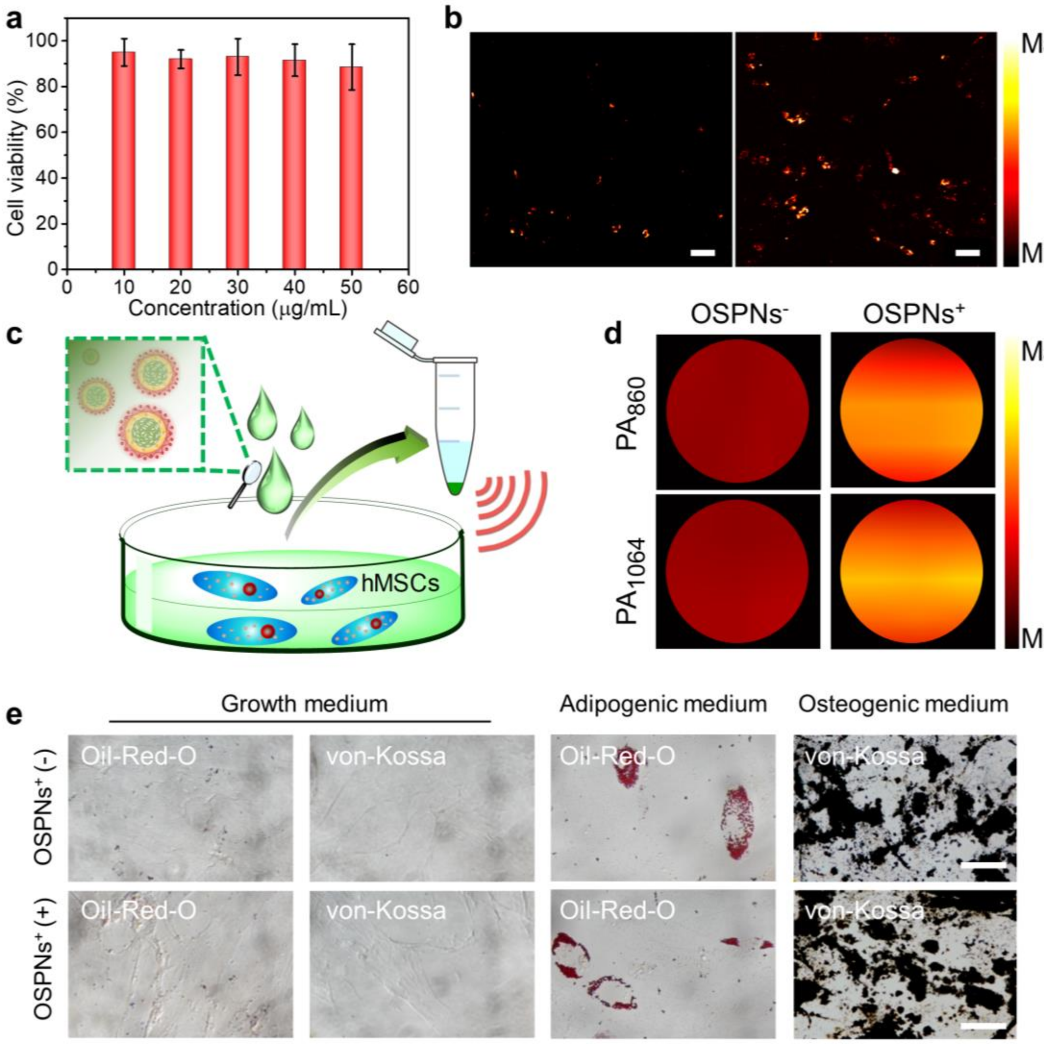

Figure 3. PA imaging of OSPNs$^+$ in hMSCs. a) The methyl thiazolyl tetrazolium (MTT) assay of hMSCs treated by OSPNs$^+$ for 12 h under various concentrations. b) PA imaging of hMSCs incubated with OSPNs$^-$ (left) and OSPNs$^+$ (right) at the same concentration of 50 μg/mL for 12 h. The excitation wavelength was fixed at 532 nm with the pulse energy of 100 nJ. Scale bar: 100 μm. c) Schematic illustration of the hMSCs incubated with OSPNs$^+$ followed by concentration for PA imaging. d) PA imaging at 860 nm (PA_{860}) and 1064 nm (PA_{1064}) of the collected hMSCs treated by OSPNs$^-$ or OSPNs$^+$. e) The influence of OSPNs$^+$ on hMSCs pluripotency. Growth medium: OSPNs$^+$-labelled hMSCs (OSPNs$^+$ (+)) and unlabelled hMSCs (OSPNs$^+$ (-)) were incubated with the growth medium for two weeks, followed by staining against

both adipogenic and osteogenic markers. Adipogenic medium: OSPNs$^+$-labelled hMSCs (OSPNs$^+$ (+)) and unlabelled hMSCs (OSPNs$^+$ (-)) were incubated with adipogenic induction medium for two weeks, followed by staining against adipogenic markers. Osteogenic medium: OSPNs$^+$-labelled hMSCs (OSPNs$^+$ (+)) and unlabelled hMSCs (OSPNs$^+$ (-)) were incubated with osteogenic induction medium for two weeks, followed by staining against osteogenic markers. Adipogenic and osteogenic differentiations were evaluated by Oil-Red-O and von-Kossa staining, respectively. Scale bar: 25 μm.

We next studied the impact of the OSPNs$^+$ on the adipogenic and osteogenic differentiations of hMSCs by using Oil-Red-O staining and von-Kossa staining, respectively. hMSCs treated with or without OSPNs$^+$ differentiated normally towards the adipogenic and osteogenic lineages when cultured in inductive media (Figure 3e). Furthermore, OSPNs$^+$ did not induce adipogenic or osteogenic differentiation of hMSCs cultured in growth medium (Figure 3e). In particular, the expression level of alkaline phosphatase (ALP), an osteogenic biomarker, was detected to quantificationally evaluate the osteogenic potential of hMSCs (Figure S15, Supporting Information). Results indicated that the ALP level of cells cultured in inductive media is ~7.5-fold higher than that of cells cultured in growth media. Furthermore, regardless of the type of media used, no significant differences in ALP activity were detected between OSPNs$^+$-labelled and unlabeled cells (Figure S15, Supporting Information). These data showed the negligible influence of the OSPNs$^+$ on the differentiation of hMSCs and their capability for *in vivo* stem cell imaging and tracking after transplantation.

We next compared NIR-II PA imaging with NIR-I PA imaging in a chicken breast tissue model. Aqueous OSPNs$^+$ solutions were prepared with three different concentrations and sealed into rubber tubes, which were subsequently covered by chicken breast tissue with tuneable thickness (Figure S16, Supporting Information). The PA signals were recorded with a lab-built PA imaging instrument, which can switch the excitation wavelength from NIR-I to NIR-II region. To compare the PA imaging capability of the OSPNs$^+$ in terms of imaging depth under both NIR light irradiation, the excitation wavelength was set to 860 nm or 1064 nm with the same intensity (5.0 mJ/cm^2). For PA imaging excited by both NIR-I and NIR-II light, the SNR decreased significantly as the imaging depth increased (achieved by increasing the thickness of covered chicken breast tissue) at all OSPNs$^+$ concentrations (Figures 4b&c). However, the NIR-II PA imaging always showed higher SNR than NIR-I PA imaging at the same concentration and imaging depth (Figure 4d). For instance, at the concentration of 0.573 mg/mL, although PA signals from both NIR light excitation can be detected at imaging depths ranging from 0.5 to 1.5 cm, NIR-II PA imaging always showed a much brighter signal than NIR-I imaging at the same tissue depth (Figure 4a). Furthermore, when the concentration was decreased to 0.286 mg/mL, the NIR-II PA signals were more visible than the NIR-I ones at 1.5-cm depth (Figure 4a). The superior performance of NIR-II over NIR-I PA imaging can be mainly attributed to scattering. Optical scattering can be effectively suppressed at longer wavelengths,[26,53,54] leading to an enhanced photon flux to the OSPNs$^+$ under the tissue. These data confirmed that the OSPNs$^+$ has a higher SNR in NIR-II than NIR-I window, making it a promising candidate for *in vivo* stem cell imaging in deep tissue.

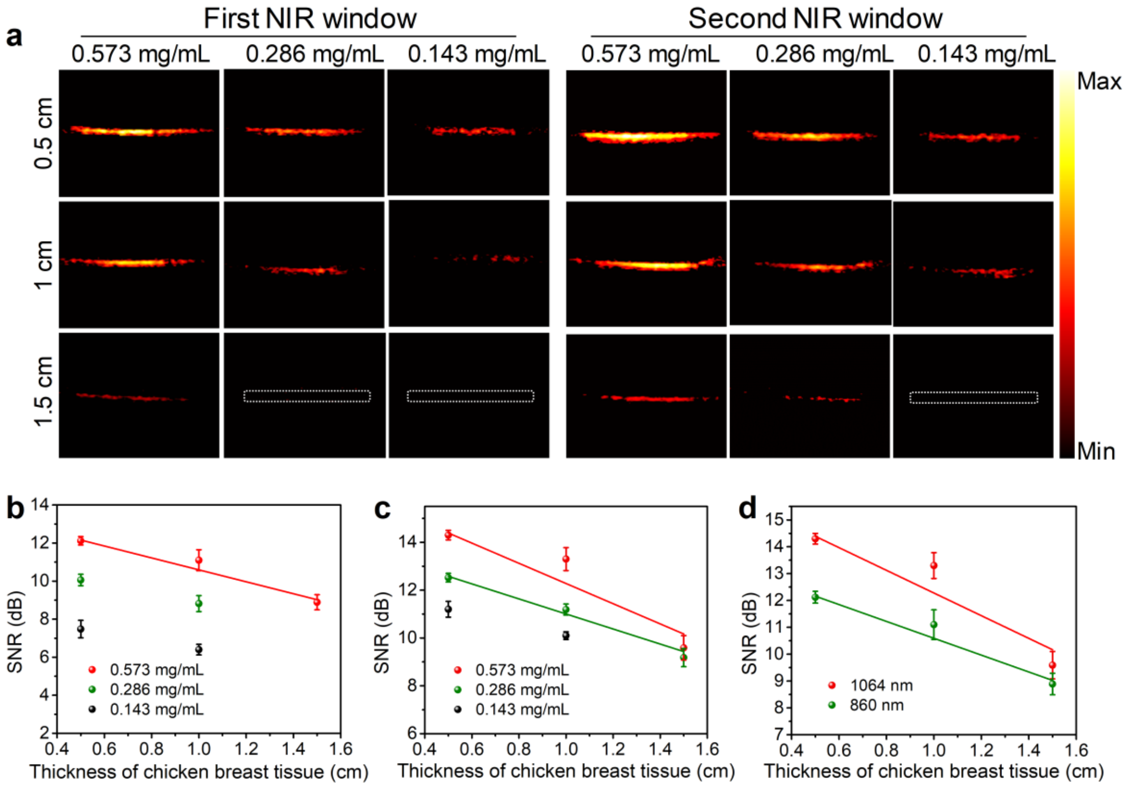

Figure 4. Comparison of NIR-I PA and NIR-II PA imaging at different imaging depths. a) PA imaging of aqueous OSPNs$^+$ solutions (0.573, 0.286, and 0.143 mg/mL) covered by chicken breast tissue with different thickness (0.5, 1.0, and 1.5 cm). Images were acquired under NIR-I laser (860 nm, left) or NIR-II laser (1064 nm, right) excitation with an identical energy density of 5.0 mJ/cm^2. b) SNR of PA imaging at 860 nm with different OSPNs$^+$ concentrations as a function of imaging depth. c) SNR of PA imaging at 1064 nm with different OSPNs$^+$ concentrations as a function of imaging depth. d) SNR of PA imaging at 860 or 1064 nm as a function of imaging depth ([OSPNs$^+$] = 0.573 mg/mL).

PA labelling and tracking of stem cells *in vivo* were demonstrated by transplanting the OSPNs$^+$-labelled hMSCs into different tissues to acquire signals at different imaging depths using a photoacoustic computed tomography (PACT) system (Figure S17, Supporting Information). For shallow tissue imaging, hMSCs incubated with or without OSPNs$^+$ were subcutaneously injected into nude mice. Immediately after cell transplantation, strong PA signals from the injected site were detected from the labelled cells with a 40.6-fold signal enhancement compared with that of the unlabelled cells (Figure 5a). Although the PA intensities diminished gradually overtime due to cell division and associated signal dilution, PA contrast was clearly visualized throughout a long period of time with just 61.4% signal attenuation at 2 weeks post-injection (Figure 5a, Figure S18, Supporting Information). This indicated that the OSPNs$^+$ can be efficiently internalized by hMSCs to emit sufficient PA signals for sensitive and long-term tracking of implanted stem cells in living mice. Besides, OSPNs$^-$ also showed the labeling ability of hMSCs for long-term PA tracking in subcutaneous tissues (Figure S19, Supporting Information). To investigate the imaging quality in deep tissues, the nude mice were intracranially injected with labelled or unlabelled cells (3 mm deep under the skull). Ultrasound (US) imaging was also performed to depict the skull profile to precisely position the implanted stem cells. The NIR-II PA signal under the skull increased significantly after the transplantation of OSPNs$^+$-labelled hMSCs with a 21.7-fold signal enhancement compared with that of the group injected with unlabelled cells (Figure 5b). In addition, because the skull and skin tissues have much lower absorption coefficient than OSPNs$^+$ at 1064 nm, no obvious PA background signals were detected, thereby showing sharp contrast of stem cell imaging in deep brain. By contrast, NIR-I PA imaging showed less signal enhancement of the OSPNs$^+$-labelled cells compared with that of unlabelled cells (Figure 5b). Quantification data revealed that the SNR value at 1064 nm was 1.38-fold higher than that at 860 nm after injection of OSPNs$^+$-labelled cells into mice brain (Figure 5c), and this corresponded well with the chicken breast tissue results, further proving the superiority of NIR-II over NIR-I PA imaging for stem cell labelling in deep brain tissues. We further performed the histological staining 14 days after injecting OSPNs$^+$-labeled stem cells to subcutaneous pocket or brain of the mice to evaluate the *in vivo* safety of the nanoparticles. Hematoxylin-eosin (H&E) staining was performed on sections obtained from tissue close to inject sites, heart, liver, spleen, lung, and kidney. Results show that no obvious anomaly of the major organs and the injection sites can be observed in both subcutaneous and brain injection groups compared with the healthy tissues/organs from animals receiving no injections (Figure S20, Supporting Information), validating the excellent biocompatibility of the nanoparticles for safe imaging and tracking in animals. The clearance ability of the nanoparticles was also evaluated by detecting their biodistribution in major organs (heart, liver, spleen, lung, and kidney) after tail vein injection for 24, 36, and 48 h. Liver exhibited much higher PA intensity at 24 h post-injection than other organs, and the PA signals from all the organs gradually decreased after 24 h post-injection and almost vanished at 2 d post-injection (Figure S21, Supporting Information). This reflected the hepatobiliary clearance process of OSPNs$^+$ which is quite similar to that for inorganic and organic nanoparticles with size larger than 10 nm.[55] These results demonstrate that OSPNs$^+$ can not only be efficiently internalized by hMSCs to generate intracellular PA signals but also show great advantages for stem cell tracking both in subcutaneous and deep brain tissues *via* NIR-II PA imaging.

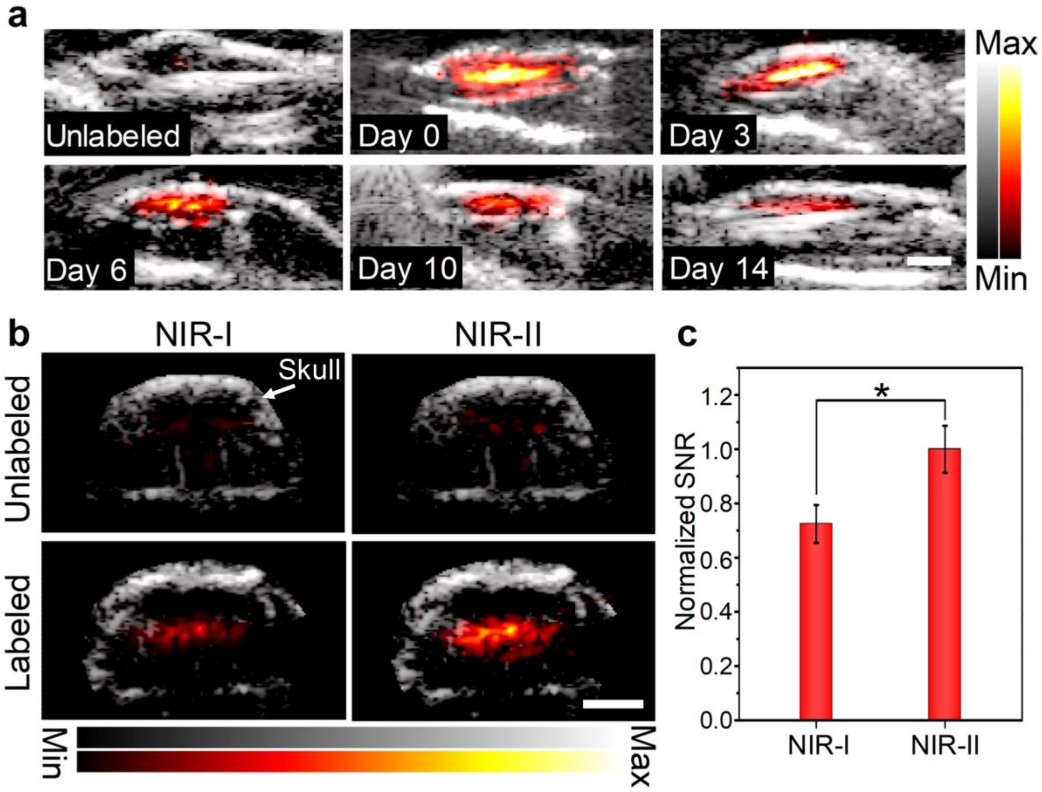

Figure 5. PA imaging *in vivo*. a) Merged ultrasound (US, grey scale) and PA (red-yellow scale) images of subcutaneously transplanted unlabelled or OSPNs$^+$-labelled hMSCs (10^5 cells). After incubation with or without OSPNs$^+$ (50 μg/mL) for 12 h, the cells were collected and mixed in 50% Matrigel/PBS (100 μL) followed by subcutaneous injection. Images of OSPNs$^+$-labelled cells were acquired serially at different post-injection time (day 0, 3, 6, 10, and 14). PA signals were recorded at 1064 nm (energy density: 5 mJ/cm^2). Scale bar: 3 mm. b) Combined US and PA imaging of unlabelled or OSPNs$^+$-labelled hMSCs (80×10^3 cells) injected into the brain of nude mice using NIR-I (860 nm) or NIR-II (1064 nm) light excitation. The energy density of the laser was adjusted to the same value at 10 mJ/cm^2. Images were collected immediately after cell injection. Arrow indicates the skull position. Scale bar: 3 mm. c) Normalized PA SNR of OSPNs$^+$-labelled hMSCs implanted into mice brain under NIR-I (860 nm) or NIR-II (1064 nm) light excitation ($*p < 0.05$).

CONCLUSIONS

In this study, we report the design and synthesis of a SP-based nanoprobe (OSPNs$^+$) for stem cells PA imaging and tracking in the NIR-II window. The OSPNs$^+$ were formulated *via* a "layer-by-layer modification" approach: hydrophobic SP was initially encapsulated using amphiphilic PSMA and then modified by PLL to produce a nanoprobe with a positively charged surface. With good biocompatibility, an appropriate size, and a superior surface property compared to the OSPNs$^-$, the OSPNs$^+$ enabled efficient PA labelling of the stem cells. Comparison studies using the chicken breast tissue model showed that NIR-II PA imaging of the OSPNs$^+$ possessed a much higher SNR relative to NIR-I PA imaging, making it a more promising candidate for deep tissue imaging. NIR-II PA labelling and tracking of the transplanted stem cells in living mice revealed obvious PA contrast enhancement by 40.6- and 21.7-fold for subcutaneous and brain imaging, respectively, compared to that of unlabelled cells. In addition, NIR-II PA imaging exhibited a higher SNR (1.38-fold) than NIR-I PA imaging in deep brain, further validating its superiority for stem cell labelling.

Our work thus demonstrates an SP-based nanoprobe with significant merits for advanced stem cell labelling and tracking. Furthermore, the structural versatility of the SP allows further development of activatable probes for real-time PA monitoring of stem cell behaviours, such as cell differentiation, which can provide more comprehensive information on stem cell fate upon transplantation and is thus a powerful tool for advancing the understanding and evaluation of stem cell-based therapy.

EXPERIMENTAL SECTION

Chemicals.

M2 was purchased from Derthon Optoelectronic Materials Science Technology Co., Ltd, Shenzhen, China. All other chemicals were purchased from Sigma-Aldrich. All the intermediates (compound 2, 3, 5, 6, and M1) were synthesized through a modified route according to the previous reports[49,50] (Supporting Information).

Characterizations.

NMR spectra were obtained from Bruker Ultra Shield Plus NMR instrument (400 MHz). Matrix-assisted laser desorption/ionization time-of-flight mass spectrometry (MALDI-TOF-MASS) was performed on a Bruker Autoflex instrument. Gel permeation chromatogram (GPC) results were obtained by a Shimadzu LC-VP system. TEM measurements were carried out using a JEOL JEM-2100 transmission electron microscope (acceleration voltage: 100.0 kV). DLS and ζ-potential results were obtained with a DelsaMax Pro Particle Sizing & Zeta Potential instrument. The absorption spectra were obtained on a Shimadzu UV-3600 UV-VIS-NIR spectrophotometer. The MTT assay was performed by a PowerWave XS/XS2 microplate spectrophotometer (BioTek, Winooski, VT).

Synthesis of SP.

M1 (0.8 g, 1.06 mmol), M2 (0.96 g, 1.06 mmol), tri(o-tolyl)phosphine (15.2 mg, 0.05 mmol), and tris(dibenzylideneacetone)dipalladium(0) (73.2 mg, 0.08 mmol) were placed in a 50-mL round-bottom flask, which was protected by nitrogen. Next, toluene (10 mL) was injected into the flask and the mixture underwent freeze-pump-thaw to further remove oxygen. Then all the precursors were heated at 100°C with stirring. After 50 min, the resulting mixture was concentrated to 1 mL to precipitate the polymer in methanol. After washing 3 times by methanol and drying, the final SP was obtained (1.32 g, yield: 75%). ^{1}H NMR ($CDCl_3$, ppm) δ: 8.94 (s, 2H), 6.54-8.12 (m, 12H), 3.97-4.43 (m, 4H), 0.70-2.09 (m, 76H). GPC result: Mn = 39800, Mw = 50100, PDI = 1.26.

Preparation of the OSPNs$^-$ and OSPNs$^+$.

The OSPNs$^-$ were synthesized through a nanoprecipitation method. In brief, THF was used to dissolve SP and poly (styrene maleic anhydride) (PSMA), and the concentration of SP and PSMA was adjusted to 40 μg/mL and 10 μg/mL, respectively. Then, the obtained THF solution (5 mL) was rapidly injected into pure water (10 mL) under sonication for 1 min (ultrasonic power: 360 W). THF was then removed by flowing nitrogen gas for 40 min. The solution was concentrated by continuous evaporation under a stream of nitrogen gas to obtain OSPNs$^-$ aqueous solution. Subsequently, 0.5 mL of poly(L-lysine) (PLL) (0.5 mg/mL) was added to the as-prepared OSPNs$^-$ aqueous solution (0.2 mL, 1 mg/mL) and stirred overnight. Then, the solution was subjected to ultrafiltration using a 100 K ultrafiltration tube to remove the excess PLL, producing the OSPNs$^+$ aqueous solution.

MTT assay.

In vitro cytotoxicity of the OSPNs$^+$ or OSPNs$^-$ was examined using human mesenchymal stem cells (hMSCs) by the MTT assay according to our previous report.[40] In brief, hMSCs (0.5×10^4 cells/well) were incubated in a 96-well plate in growth medium. Different concentrations of OSPNs$^+$ or OSPNs$^-$ were used to culture the cells for 12 h. After that, 10 μL MTT (0.5 mg/mL) was added to each well to produce formazan crystals, which were further dissolved by 200 μL of DMSO. Finally, a microplate reader was used to collect the absorbance value of each well for cell viability calculation.

In vitro cell differentiation.

For the growth medium group, $OSPNs^+$-labelled (50 μg/mL) or -unlabelled hMSCs were cultured in the growth medium for two weeks. Afterwards, the cells were stained with Oil-Red-O or a von-Kossa staining kit. For the adipogenic medium group, the $OSPNs^+$-labelled (50 μg/mL) or -unlabelled hMSCs were cultured in the adipogenic induction medium for two weeks. Afterwards, the cells were stained with Oil-Red-O. For the osteogenic medium group, the $OSPNs^+$-labelled (50 μg/mL) or -unlabelled hMSCs were cultured in the osteogenic induction medium for two weeks. Afterwards, the cells were stained with von-Kossa staining kit.

To detect the alkaline phosphatase (ALP) level of hMSCs, cells were cultured in growth medium or osteogenic induction medium with or without $OSPNs^+$. After incubating for 14 days, cells were collected to detect the ALP activity by using the ALP detection kit carefully following manufacturer's guidelines.

Photoacoustic instrument.

To test the photoacoustic imaging ability of the $OSPNs^+$ *in vitro*, an optical-resolution photoacoustic microscopy (OR-PAM) system based on a 532 nm nanosecond pulsed laser was exploited to collectmaximum-amplitude-projection (MAP) imaging. The highest pulse repetition rate of this laser is 1 MHz, while the average power is 20 W. During experiments, the selected pulse width is 7 ns and the pulse repetition rate is 10 kHz. By using a neutral density filter, the final output laser beam energy is controlled to 100 nJ, which is enough to image the nanoparticle samples and cells. Two stepper motors are involved to perform the 2D scanning. During the imaging of the samples, 2000×2000 A-lines with 5 Hz are acquired to compare the average photoacoustic amplitude.

A photoacoustic computed tomography (PACT) was constructed to perform the photoacoustic imaging *in vivo*. A tuneable optical parametric oscillator (OPO) system (basiScan-M/120/HE, Spectral-Physics) pumped by an Nd:YAG laser (Quanta-Ray, INDI-40-20, Spectra-Physics, Santa Clara, California) provided the irradiation pulses. The laser pulse width was approximately 6 to 9 ns at full width at half maximum (FWHM). The pulse repetition rate was 20 Hz with the wavelength tuned from 400 to 2000 nm. The light was delivered by a 1 mm diameter fibre, and the energy density was lower than the American National Standards Institute (ANSI) safety limit. The photoacoustic signal was received with an L11-4v transducer array (a 128-element linear transducer array with 6.25 MHz central frequency, Verasonics). The photoacoustic signals received by the transducer array were digitized by a 128-channel ultrasound data acquisition (DAQ) system (Vantage, Verasonics).

Photoacoustic (PA) imaging of the hMSCs.

The hMSCs (10^5 cells/well) were cultured in a six-well plate for 24 h. After removing the culture medium and washing the adherent cells for three times, the cells were incubated with growth medium containing the indicated concentration of OSPNs^- or OSPNs^+ (50 μg/mL). After 12 h, the cells were washed with PBS buffer and imaged in the OR-PAM. The excitation wavelength was fixed at 532 nm with a pulse energy of 100 nJ. For cell pellet imaging, the hMSCs (100×10^3 cells) were treated with OSPNs$^-$ or OSPNs$^+$ (50 μg/mL) for 12 h and then washed and collected by centrifugation. After that, the labeled cells were dispersed in Matrigel to monitor their PA emissions on the PACT instrument using both the 860 and 1064 nm lasers for excitation (5 mJ/cm^2).

Quantification of cellular uptake.

For the cellular uptake investigation, we designed and carried out the experimental procedure as follows: hMSCs (10^5 cells) were first incubated with OSPNs$^+$ or OSPNs$^-$ (50 μg/mL, 1 mL) for 12 h. The amount of added nanoparticles was 500 pg/cell. After 12 h incubation, the cells were washed with PBS buffer three times and then treated with trypsin. Next, the cell suspension was centrifuged to collect the nanoparticle-labelled cells. Subsequently, the cell pellet was resuspended in pure water (1 mL) and treated with ultrasonic agitation to break the cells. After centrifugation, the supernatant containing nanoparticles internalized by hMSCs was collected for absorbance measurement at 1025 nm (Abs. = 0.013). Based on the linear fitting formula calculated from the plot of absorbance at 1025 nm *versus* nanoparticles concentrations (Figure S10, Supporting Information), the concentration of OSPNs$^+$ dispersed in supernatant can be calculated as 12.75 μg/mL. Therefore, the average number of internalized nanoparticles into one single cell can be calculated as follows:

$$(12.75\ \mu\text{g/mL} \times 1\ \text{mL})/10^5\ \text{cells} = 127.5\ \text{pg/cell}$$

Thus, the hMSCs internalized about 25.5% of the added OSPNs$^+$ (500 pg/cell).

In a similar way, the internalized amount of OSPNs$^-$ in a single cell was estimated to be 39.6 pg/cell (7.92% of the added nanoparticles), which was only about one third of that of OSPNs$^+$.

Chicken breast tissue model.

The OSPNs$^+$ aqueous solution with three different concentrations (0.143, 0.286, and 0.573 mg/mL) were prepared and sealed into rubber tubes, which were fixed on a plastic plate. Then, chicken breast tissue with various thicknesses (0.5, 1.0, and 1.5 cm) was used to cover the plate. Photoacoustic imaging was carried out using the PACT instrument under both 860 nm and 1064 nm laser excitation with an identical energy density of 5.0 mJ/cm^2.

PA imaging *in vivo*.

Adult male nude mice purchased from the Laboratory Animal Services Centre of the Chinese University of Hong Kong were used in this study. All the procedures were approved by the Animal Experimental Ethical Committee of the Chinese University of Hong Kong before performing this experiment. After anaesthetization, unlabelled or OSPNs$^+$/OSPNs$^-$-labelled hMSCs (10^5 cells) in 50% Matrigel/PBS (100 μL) were injected subcutaneously into the mice and imaged using the PACT system. Images of the OSPNs$^+$/OSPNs$^-$-labelled cells were recorded serially at different post-injection times (day 0, 3, 6, 10, and 14). PA images were acquired in PACT system under 1064 nm laser excitation (5 mJ/cm^2). For deep tissue imaging, 80×10^3 OSPNs$^+$-labelled or -unlabelled hMSCs suspended in PBS (10 μL) were injected into the brain using a cranial stereotactic frame instrument. The parameter was set as follows: Anterior/Posterior: 0.110, Medial/Lateral: -2.290, Dorsal/Ventral: -3.000. The PA imaging was conducted in the PACT system under 860 or 1064 nm laser excitation with the same energy density of 10 mJ/cm^2. For biodistribution study, mice were treated with OSPNs$^+$ (120 μL, 0.1 mg/mL) through tail vein injection. After 24, 36, and 48 h post-injection, mice were sacrificed by CO_2 asphyxiation, and major organs were excised to detect the PA signal at 1064 nm using PACT instrument.

Histological investigation.

Histological studies were performed to evaluate the *in vivo* safety of the OSPNs$^+$. The experiment was separated into three groups. For the subcutaneously implanted mouse at 14 days post-injection, H&E staining of subcutaneous tissues (close to the stem cell injected site), heart, liver, spleen, lung, and kidney were conducted; for the brain implanted mouse at 14 days post-injection, H&E staining of brain tissues (close to the stem cell injected site), heart, liver, spleen, lung, and kidney were conducted; for the control group, H&E staining of brain tissues, subcutaneous tissues, heart, liver, spleen, lung, and kidney were carried out.

Data analysis.

The intensities of the photoacoustic signal were determined by region-of-interest analysis using MATLAB. GraphPad Prism (GraphPad Software Inc., CA) was used to conduct all the data analysis.

ASSOCIATED CONTENT

Supporting Information Available: NMR and MALDI-TOF mass spectrum of monomer 1, ^{1}H NMR and GPC results of the SP, TEM of OSPNs$^-$, structural stability and detailed optical performance of OSPNs$^+$, photostability of OSPNs$^+$, MTT assay of

OSPNs$^-$, cell uptake of OSPNs$^+$ and OSPNs$^-$, ALP activity detection, chicken breast tissue model, PACT instrument, PA signal quantification of OSPNs$^+$-labelled stem cells subcutaneously implanted into nude mice at different post-injection times, long-term PA tracking of stem cells using OSPNs$^-$, *in vivo* safety of OSPNs$^+$, and biodistribution of OSPNs$^+$ in major organs (Figures S1-S21)

This material is available free of charge *via* the Internet at http://pubs.acs.org.

The authors declare no competing financial interest.

AUTHOR INFORMATION

Corresponding Authors

*E-mail: kypu@ntu.edu.sg
*E-mail: lidawang@cityu.edu.hk
*E-mail: lbian@cuhk.edu.hk

Author Contributions

The manuscript was written through contributions of all authors. All authors have given approval to the final version of the manuscript.
‖ C.Y., G.W., and C.L. contributed equally to this work.

ACKNOWLEDGMENTS

Project 31570979 is supported by the National Natural Science Foundation of China. This work is supported by a General Research Fund grant from the Research Grants Council of Hong Kong (project no. 14220716); the Health and Medical Research Fund, the Food and Health Bureau, the Government of the Hong Kong Special Administrative Region (reference no.: 04152836); the Chow Yuk Ho Technology Centre for Innovative Medicine, The Chinese University of Hong Kong.

L.W. thanks the Research Grants Council of the Hong Kong Special Administrative Region (ECS 21205016, and GRF 11215817), City University of Hong Kong startup grant (9610339), Shenzhen (China) Basic Research Project (JCYJ20160329150236426, JCYJ20170413140519030), and National Natural Science Foundation of China (NSFC) (81627805) for the financial support.

K.P. thanks Nanyang Technological University (Start-up grant: NTU-SUG: M4081627.120) and Singapore Ministry of Education, Academic Research Fund Tier

1 (2017-T1-002-134-RG147/17) and Academic Research Fund Tier 2 (MOE2016-T2-1-098) for the financial support.

REFERENCES

(1) Pittenger, M. F.; Mackay, A. M.; Beck, S. C.; Jaiswal, R. K.; Douglas, R.; Mosca, J. D.; Moorman, M. A.; Simonetti, D. W.; Craig, S.; Marshak, D. R. Multilineage Potential of Adult Human Mesenchymal Stem Cells. *Science* **1999**, *284*, 143-147.

(2) Wang, S.; Qu, X.; Zhao, R. C. Clinical Applications of Mesenchymal Stem Cells. *J. Hematol. Oncol.* **2012**, *5*, 19.

(3) Barry, F. P.; Murphy, J. M. Mesenchymal Stem Cells: Clinical Applications and Biological Characterization. *Int. J. Biochem. Cell Biol.* **2004**, *36*, 568-584.

(4) Mazza, M.; Lozano, N.; Vieira, D. B.; Buggio, M.; Kielty, C.; Kostarelos, K. Liposome-Indocyanine Green Nanoprobes for Optical Labeling and Tracking of Human Mesenchymal Stem Cells Post-Transplantation *In Vivo*. *Adv. Healthcare Mater.* **2017**, *6*, 1700374.

(5) Li, J.; Lee, W. Y.; Wu, T.; Xu, J.; Zhang, K.; Li, G.; Xia, J.; Bian, L. Multifunctional Quantum Dot Nanoparticles for Effective Differentiation and Long-Term Tracking of Human Mesenchymal Stem Cells *In Vitro* and *In Vivo*. *Adv. Healthcare Mater.* **2016**, *5*, 1049-1057.

(6) Chen, D.; Li, Q.; Meng, Z.; Guo, L.; Tang, Y.; Liu, Z.; Yin, S.; Qin, W.; Yuan, Z.; Zhang, X.; Wu, C. Bright Polymer Dots Tracking Stem Cell Engraftment and Migration to Injured Mouse Liver. *Theranostics* **2017**, *7*, 1820-1834.

(7) Ngen, E. J.; Wang, L.; Kato, Y.; Krishnamachary, B.; Zhu, W.; Gandhi, N.; Smith,

B.; Armour, M.; Wong, J.; Gabrielson, K.; Artemov, D. Imaging Transplanted Stem Cells in Real Time Using an MRI Dual-Contrast Method. *Sci. Rep.* **2015**, *5*, 13628.

(8) Nejadnik, H.; Castillo, R.; Daldrup-Link, H. E. Magnetic Resonance Imaging and Tracking of Stem Cells. *Methods Mol. Biol.* **2013**, *1052*, 167-176.

(9) Lemaster, J. E.; Chen, F.; Kim, T.; Hariri, A.; Jokerst, J. V. Development of a Trimodal Contrast Agent for Acoustic and Magnetic Particle Imaging of Stem Cells. *ACS Appl. Nano Mater.* **2018**, *1*, 1321-1331.

(10) Sun, X.; Cai, W.; Chen, X. Positron Emission Tomography Imaging Using Radiolabeled Inorganic Nanomaterials. *Acc. Chem. Res.* **2015**, *48*, 286-294.

(11) Cao, F.; Lin, S.; Xie, X.; Ray, P.; Patel, M.; Zhang, X.; Drukker, M.; Dylla, S. J.; Connolly, A. J.; Chen, X.; Weissman, I. L.; Gambhir, S. S.; Wu, J. C. *In Vivo* Visualization of Embryonic Stem Cell Survival, Proliferation, and Migration After Cardiac Delivery. *Circulation* **2006**, *113*, 1005-1014.

(12) Bulte, J. W. M.; Douglas, T.; Witwer, B.; Zhang, S. C.; Strable, E.; Lewis, B. K.; Zywicke, H.; Miller, B.; van Gelderen, P.; Moskowitz, B. M.; Duncan, I. D.; Frank, J. A. Magnetodendrimers Allow Endosomal Magnetic Labeling and *In Vivo* Tracking of Stem Cells. *Nat. Biotechnol.* **2001**, *19*, 1141-1147.

(13) Duan, X. H.; Wang, Y.; Zhang, F.; Lu, L. J.; Cao, M. H.; Lin, B. L.; Zhang, X.; Mao, J. J.; Shuai, X. T.; Shen, J. Superparamagnetic Iron Oxide-Loaded Cationic Polymersomes for Cellular MR Imaging of Therapeutic Stem Cells in Stroke. *J. Biomed. Nanotechnol.* **2016**, *12*, 2112-2124.

(14) Kim, T.; Lemaster, J. E.; Chen, F.; Li, J.; Jokerst, J. V. Photoacoustic Imaging of

Human Mesenchymal Stem Cells Labeled with Prussian Blue-Poly(L-lysine) Nanocomplexes. *ACS Nano* **2017**, *11*, 9022-9032.

(15) Wang, L. V.; Hu, S. Photoacoustic Tomography: *In vivo* Imaging from Organelles to Organs. *Science* **2012**, *335*, 1458-1462.

(16) Yang, Z.; Tian, R.; Wu, J.; Fan, Q.; Yung, B. C.; Niu, G.; Jacobson, O.; Wang, Z.; Liu, G.; Yu, G.; Huang, W.; Song, J.; Chen, X. Impact of Semiconducting Perylene Diimide Nanoparticle Size on Lymph Node Mapping and Cancer Imaging. *ACS Nano* **2017**, *11*, 4247-4255.

(17) Jiang, Y.; Pu, K. Advanced Photoacoustic Imaging Applications of Near-Infrared Absorbing Organic Nanoparticles. *Small* **2017**, *13*, 1700710.

(18) Jiang, Y.; Upputuri, P. K.; Xie, C.; Lyu, Y.; Zhang, L.; Xiong, Q.; Pramanik, M.; Pu, K. Broadband Absorbing Semiconducting Polymer Nanoparticles for Photoacoustic Imaging in Second Near-Infrared Window. *Nano Lett.* **2017**, *17*, 4964-4969.

(19) Yin, C.; Tang, Y.; Li, X.; Yang, Z.; Li, J.; Li, X.; Huang, W.; Fan, Q. A Single Composition Architecture-Based Nanoprobe for Ratiometric Photoacoustic Imaging of Glutathione (GSH) in Living Mice. *Small* **2018**, *14*, 1703400.

(20) Li, L. L.; Ma, H. L.; Qi, G. B.; Zhang, D.; Yu, F.; Hu, Z.; Wang, H. Pathological-Condition-Driven Construction of Supramolecular Nanoassemblies for Bacterial Infection Detection. *Adv. Mater.* **2016**, *28*, 254-262.

(21) Liu, Y.; Wang, S.; Ma, Y.; Lin, J.; Wang, H. Y.; Gu, Y.; Chen, X.; Huang, P. Ratiometric Photoacoustic Molecular Imaging for Methylmercury Detection in Living

Subjects. *Adv. Mater.* **2017**, *29*, 1606129.

(22) Ntziachristos, V.; Razansky, D. Molecular Imaging by Means of Multispectral Optoacoustic Tomography (MSOT). *Chem. Rev.* **2010**, *110*, 2783-2794.

(23) Comenge, J.; Fragueiro, O.; Sharkey, J.; Taylor, A.; Held, M.; Burton, N. C.; Park, B. K.; Wilm, B.; Murray, P.; Brust, M.; Lévy, R. Preventing Plasmon Coupling Between Gold Nanorods Improves the Sensitivity of Photoacoustic Detection of Labeled Stem Cells *In Vivo*. *ACS Nano* **2016**, *10*, 7106-7116.

(24) Nam, S. Y.; Ricles, L. M.; Suggs, L. J.; Emelianov, S. Y. *In Vivo* Ultrasound and Photoacoustic Monitoring of Mesenchymal Stem Cells Labeled with Gold Nanotracers. *Plos One* **2012**, *7*, e37267.

(25) Jokerst, J. V.; Thangaraj, M.; Kempen, P. J.; Sinclair, R.; Gambhir, S. S. Photoacoustic Imaging of Mesenchymal Stem Cells in Living Mice *via* Silica-Coated Gold Nanorods. *ACS Nano* **2012**, *6*, 5920-5930.

(26) Guo, B.; Sheng, Z.; Kenry; Hu, D.; Lin, X.; Xu, S.; Liu, C.; Zheng, H.; Liu, B. Biocompatible Conjugated Polymer Nanoparticles for Highly Efficient Photoacoustic Imaging of Orthotopic Brain Tumors in the Second Near-Infrared Window. *Mater. Horiz.* **2017**, *4*, 1151-1156.

(27) Lyu, Y.; Pu, K. Recent Advances of Activatable Molecular Probes Based on Semiconducting Polymer Nanoparticles in Sensing and Imaging. *Adv. Sci.* **2017**, *4*, 1600481.

(28) Zhu, C. L.; Liu, L. B.; Yang, Q.; Lv, F. T.; Wang, S. Water-Soluble Conjugated Polymers for Imaging, Diagnosis, and Therapy. *Chem. Rev.* **2012**, *112*, 4687-4735.

(29) Wu, C.; Chiu, D. T. Highly Fluorescent Semiconducting Polymer Dots for Biology and Medicine. *Angew. Chem. Int. Ed.* **2013**, *52*, 3086-3109.

(30) Pu, K.; Shuhendler, A. J.; Rao, J. Semiconducting Polymer Nanoprobe for *In Vivo* Imaging of Reactive Oxygen and Nitrogen Species. *Angew. Chem. Int. Ed.* **2013**, *52*, 10325-10329.

(31) Jiang, Y.; Li, J.; Zhen, X.; Xie, C.; Pu, K. Dual-Peak Absorbing Semiconducting Copolymer Nanoparticles for First and Second Near-Infrared Window Photothermal Therapy: A Comparative Study. *Adv. Mater.* **2018**, *30*, 1705980.

(32) Yin, C.; Zhu, H.; Xie, C.; Zhang, L.; Chen, P.; Fan, Q.; Huang, W.; Pu, K. Organic Nanoprobe Cocktails for Multilocal and Multicolor Fluorescence Imaging of Reactive Oxygen Species. *Adv. Funct. Mater.* **2017**, *27*, 1700493.

(33) Zhu, H.; Fang, Y.; Zhen, X.; Wei, N.; Gao, Y.; Luo, K. Q.; Xu, C.; Duan, H.; Ding, D.; Chen, P.; Pu, K. Multilayered Semiconducting Polymer Nanoparticles with Enhanced NIR Fluorescence for Molecular Imaging in Cells, Zebrafish and Mice. *Chem. Sci.* **2016**, *7*, 5118-5125.

(34) Chen, D.; Wu, I. C.; Liu, Z.; Tang, Y.; Chen, H.; Yu, J.; Wu, C.; Chiu, D. T. Semiconducting Polymer Dots with Bright Narrow-Band Emission at 800 nm for Biological Applications. *Chem. Sci.* **2017**, *8*, 3390-3398.

(35) Ke, C. S.; Fang, C. C.; Yan, J. Y.; Tseng, P. J.; Pyle, J. R.; Chen, C. P.; Lin, S. Y.; Chen, J.; Zhang, X.; Chan, Y. H. Molecular Engineering and Design of Semiconducting Polymer Dots with Narrow-Band, Near-Infrared Emission for *in Vivo* Biological Imaging. *ACS Nano* **2017**, *11*, 3166-3177.

(36) Zhen, X.; Zhang, C.; Xie, C.; Miao, Q.; Lim, K. L.; Pu, K. Intraparticle Energy Level Alignment of Semiconducting Polymer Nanoparticles to Amplify Chemiluminescence for Ultrasensitive *In Vivo* Imaging of Reactive Oxygen Species. *ACS Nano* **2016**, *10*, 6400-6409.

(37) Shuhendler, A. J.; Pu, K.; Cui, L.; Uetrecht, J. P.; Rao, J. Real-Time Imaging of Oxidative and Nitrosative Stress in the Liver of Live Animals for Drug-Toxicity Testing. *Nat. Biotechnol.* **2014**, *32*, 373-380.

(38) Miao, Q.; Xie, C.; Zhen, X.; Lyu, Y.; Duan, H.; Liu, X.; Jokerst, J. V.; Pu, K. Molecular Afterglow Imaging with Bright, Biodegradable Polymer Nanoparticles. *Nat. Biotechnol.* **2017**, *35*, 1102-1110.

(39) Xie, C.; Zhen, X.; Miao, Q.; Lyu, Y.; Pu, K. Self-Assembled Semiconducting Polymer Nanoparticles for Ultrasensitive Near-Infrared Afterglow Imaging of Metastatic Tumors. *Adv. Mater.* **2018**, *30*, 1801331.

(40) Yin, C.; Zhen, X.; Fan, Q.; Huang, W.; Pu, K. Degradable Semiconducting Oligomer Amphiphile for Ratiometric Photoacoustic Imaging of Hypochlorite. *ACS Nano* **2017**, *11*, 4174-4182.

(41) Yin, C.; Zhen, X.; Zhao, H.; Tang, Y.; Ji, Y.; Lyu, Y.; Fan, Q.; Huang, W.; Pu, K. Amphiphilic Semiconducting Oligomer for Near-Infrared Photoacoustic and Fluorescence Imaging. *ACS Appl. Mater. Interfaces* **2017**, *9*, 12332-12339.

(42) Pu, K.; Shuhendler, A. J.; Jokerst, J. V.; Mei, J.; Gambhir, S. S.; Bao, Z.; Rao, J. Semiconducting Polymer Nanoparticles as Photoacoustic Molecular Imaging Probes in Living Mice. *Nat. Nanotechnol.* **2014**, *9*, 233-239.

(43) Guo, B.; Sheng, Z.; Hu, D.; Li, A.; Xu, S.; Manghnani, P. N.; Liu, C.; Guo, L.; Zheng, H.; Liu, B. Molecular Engineering of Conjugated Polymers for Biocompatible Organic Nanoparticles with Highly Efficient Photoacoustic and Photothermal Performance in Cancer Theranostics. *ACS Nano* **2017**, *11*, 10124-10134.

(44) Yang, Z.; Dai, Y.; Yin, C.; Fan, Q.; Zhang, W.; Song, J.; Yu, G.; Tang, W.; Fan, W.; Yung, B. C.; Li, J.; Li, X.; Li, X.; Tang, Y.; Huang, W.; Song, J.; Chen, X. Activatable Semiconducting Theranostics: Simultaneous Generation and Ratiometric Photoacoustic Imaging of Reactive Oxygen Species *In Vivo*. *Adv. Mater.* **2018**, *30*, 1707509.

(45) Yang, K.; Xu, H.; Cheng, L.; Sun, C.; Wang, J.; Liu, Z. *In Vitro* and *In Vivo* Near-Infrared Photothermal Therapy of Cancer Using Polypyrrole Organic Nanoparticles. *Adv. Mater.* **2012**, *24*, 5586-5592.

(46) Sun, T.; Dou, J. H.; Liu, S.; Wang, X.; Zheng, X.; Wang, Y.; Pei, J.; Xie, Z. Second Near-Infrared Conjugated Polymer Nanoparticles for Photoacoustic Imaging and Photothermal Therapy. *ACS Appl. Mater. Interfaces* **2018**, *10*, 7919-7926.

(47) Zhu, H.; Fang, Y.; Miao, Q.; Qi, X.; Ding, D.; Chen, P.; Pu, K. Regulating Near-Infrared Photodynamic Properties of Semiconducting Polymer Nanotheranostics for Optimized Cancer Therapy. *ACS Nano* **2017**, *11*, 8998-9009.

(48) Qin, X.; Chen, H.; Yang, H.; Wu, H.; Zhao, X.; Wang, H.; Chour, T.; Neofytou, E.; Ding, D.; Daldrup-Link, H.; Heilshorn, S. C.; Li, K.; Wu, J. C. Photoacoustic Imaging of Embryonic Stem Cell-Derived Cardiomyocytes in Living Hearts with Ultrasensitive Semiconducting Polymer Nanoparticles. *Adv. Funct. Mater.* **2018**, *28*,

1704939.

(49) Secondo, P.; Fages, F. Design and Synthesis of Bismacrocyclic Hexaazatriphenylene Derivatives. *Org. Lett.* **2006**, *8*, 1311-1314.

(50) Liu, J.; Geng, J.; Liao, L. D.; Thakor, N.; Gao, X.; Liu, B. Conjugated Polymer Nanoparticles for Photoacoustic Vascular Imaging. *Polym. Chem.* **2014**, *5*, 2854-2862.

(51) Babič, M.; Horák, D.; Trchová, M.; Jendelová, P.; Glogarová, K.; Lesný, P.; Herynek, V.; Hájek, M.; Syková, E. Poly(L-lysine)-Modified Iron Oxide Nanoparticles for Stem Cell Labeling. *Bioconjugate Chem.* **2008**, *19*, 740-750.

(52) Pongrac, I. M.; Dobrivojević, M.; Ahmed, L. B.; Babič, M.; Šlouf, M.; Horák, D.; Gajović, S. Improved Biocompatibility and Efficient Labeling of Neural Stem Cells with Poly(L-lysine)-Coated Maghemite Nanoparticles. *Beilstein J. Nanotechnol.* **2016**, *7*, 926-936.

(53) Ku, G.; Zhou, M.; Song, S.; Huang, Q.; Hazle, J.; Li, C. Copper Sulfide Nanoparticles as a New Class of Photoacoustic Contrast Agent for Deep Tissue Imaging at 1064 nm. *ACS Nano* **2012**, *6*, 7489-7496.

(54) Allen, T. J.; Hall, A.; Dhillon, A. P.; Owen, J. S.; Beard, P. C. Spectroscopic Photoacoustic Imaging of Lipid-Rich Plaques in the Human Aorta in the 740 to 1400 nm Wavelength Range. *J. Biomed. Opt.* **2012**, *17*, 061209.

(55) Longmire, M.; Choyke, P. L.; Kobayashi, H. Clearance Properties of Nano-Sized Particles and Molecules as Imaging Agents: Considerations and Caveats. *Nanomedicine* **2008**, *3*, 703-717.

Table of Contents Graphic